UAV Image Mosaicking Based on Multiregion Guided Local Projection Deformation

Quan Xu, Jun Chen, Linbo Luo, Wenping Gong, and Yong Wang

***Abstract*—The goal of unmanned aerial vehicle (UAV) image mosaicking is to create natural- looking mosaics without artifacts due to the parallax of the image and relative camera motion. UAV remote sensing is a low-altitude technology and the UAV imaged scene is not effectively planar, yielding parallax on the images. Moreover, when an object in 3-D is mapped to an image plane, different surfaces have different projections. These projections vary with the viewpoint in a sequence of UAV images, which causes artifacts near some tall buildings in the stitched images. To solve these problems, we propose a novel stitching method based on multiregion guided local projection deformation, which can significantly reduce ghosting due to these projections vary with the viewpoint and the parallax. In the proposed method, the image is initially meshed and each cell corresponds to a local homography for image matching, which can reduce misalignment artifacts in the results compared with 2-D projective transforms or global homography. Then, we divide the overlapping regions of input images into multiple regions by classifying feature points. The partitioned regions which serve well scene constraints, are employed to guide the calculation of local homography. Specifically, instead of calculating local homography by the distance between all the feature points in the image and the vertices of the grid, we propose a strategy where multiple regions have different weights for calculating local homography, which can significantly reduce ghosting near some tall buildings. The benefits of the proposed approach are demonstrated using a variety of challenging cases.**

***Index Terms*—Image matching, local projection, multiple regions, Unmanned aerial vehicle (UAV) image mosaicking.**

I. Introduction

UNMANNED aerial vehicle (UAV) has many functions such as automatic take-off and landing, automatic driving, automatic navigation, automatic fast and accurate positioning, automatic information collection and transmission, etc. It is especially suitable for replacing human to complete tasks in difficult, harsh, or extreme environments. It has been widely used in various ground survey applications [1]. However, due to the limitations of the imaging width or mechanism, it is difficult to include full region of interest in a remote sensing image scene [2]. Image stitching is a technique of forming a mosaic by combining overlapping areas of multiple images [3]–[6]. In addition, image stitching is very important because it is required for many real world tasks, including remote sensing image processing [7], [8], resource and environmental monitoring [9], [10], and so on.

Most image stitching methods have the same steps, first calculating the alignment function of the overlapping areas of the images, and then projecting the aligned images onto a common canvas [11]. Of course, it is difficult to achieve perfect alignment in real life, so many studies are devoted to designing better alignment functions or synthesis techniques to reduce or hide the misaligned artifact areas. We also focus on the first part and hope to acquire a robust projection model to align the image. Autostitch [12] is a classical image stitching algorithm and models the alignment functions as global homography. Global homography is valid only if the images are obtained purely by camera rotation only, or if the imaged scene is effectively planar. However, UAV images may not be on a plane, and Autostitch will appear artifacts for the case of a certain parallax, which seriously affects the stitching effect. Since the global transformation cannot meet these requirements, several space-varying transformation models are proposed, of which the as-projective-as-possible (APAP) [13] warp is representative. APAP meshes images, and computes a local homography for every image cell to achieve high-precision local alignment. This method is more robust compared with global homography.

There are two challenges in UAV image stitching. On the one hand, it is common situation that the UAV images may not be on a plane, yielding parallax on the images. On the other hand, when an object in 3-D is mapped to an image plane, different surfaces have different projections and these projections vary with the viewpoint in a sequence of UAV images, which causes some artifacts in mosaic. A practical example is shown in Fig. 1. With the change of viewpoint, the scenery in the red, yellow, blue, and green boxes has obvious changes. Thus, the pixels in different target surfaces should be warped by using different transformation models for the alignment of the two images with different viewpoints. Reconstruction 3-D surface based on SFM can solve the problem of projecting different planes, but only for dense data.

Manuscript received May 7, 2020; revised June 10, 2020; accepted June 24, 2020. Date of publication July 1, 2020; date of current version July 13, 2020. This work was supported by the National Natural Science Foundation of China under Grant 41977242 and Grant 61973283. *(Corresponding author: Jun Chen.)*

Quan Xu, Linbo Luo, and Yong Wang are with the School of Mechanical Engineering and Electronic Information, China University of Geosciences, Wuhan 430074, China (e-mail: xuquan950519@cug.edu.cn; luolb@ige-live.com; yongwang_cug@163.com).

Jun Chen is with the School of Automation, Hubei Key Laboratory of Advanced Control and Intelligent Automation for Complex Systems, China University of Geosciences, Wuhan 430074, China (e-mail: chenjun71983@163.com).

Wenping Gong is with the Faculty of Engineering, China University of Geosciences, Wuhan 430074, China (e-mail: wenpinggong@cug.edu.cn).

Digital Object Identifier 10.1109/JSTARS.2020.3006289

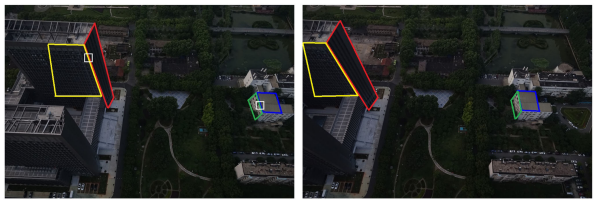

Fig. 1. Two images are captured with different viewpoints, and the same planar scenery is covered by the boxes of the same color in the two images.

In this article, we propose a novel stitching method based on multiregion guided local projection deformation, which can significantly reduces ghosting due to the parallax and these projections vary with the viewpoint. We address the first challenge by applying local projection model. The local projection model has a high degree of freedom and is flexible, which can handle local transformation and reduce artifacts. For the second challenge, we improve the local projection model and propose multiregion guided local projection deformation, which makes full use of the structure information of the image to obtain an accurate matching. We divide the overlapping regions of input images into multiple regions by classifying feature points. The partitioned regions which serve well scene constraints, are employed to guide the calculation of local homography. If we just divide an input image into a number of fixed-size cells and compute the local homography by the distance between all the feature points in the image and the vertices of the grid, the pixels within the same cell are then warped using the same local transformation model for the alignment. It is not very rigorous and the transformation models in one cell may not be consistent. For example, the scenery in the white cell should be warped by using different transformation models in Fig. 1. If all feature points are considered as a whole to calculate the weight, the projection model in the white cell should be consistent, which is inconsistent with the actual object structure information and will form ghostly effects in the stitching results. We propose a strategy where multiple regions have different weights and the region close to the cell has a large weight distribution for calculating local homography, which can significantly reduces ghosting near some tall buildings. Our method is more robust to the challenges mentioned.

The major contributions of this work are summarized in three aspects. First, we use local projection model to address the challenge of UAV image mosaicking that images may not be on a plane. Second, we propose multiregion guided local projection deformation by making use of the structure information of the image to address the challenge that these projections vary with the viewpoint. Third, we propose a strategy where multiple regions have different weights for calculating local homography, which obtains an accurate alignment in overlapping regions.

The rest of this article is organized as follows. Section II introduces some related works about image stitching. Section III describes the proposed method in detail. The experimental results are presented in Section IV. Section V concludes this article.

II. Related Work

This section briefly reviews the background material on which our work is based, including remote sensing image mosaicking, description of deformation model and seam cutting.

A. Remote Sensing Image Mosaicking

Remote sensing image mosaicking has a long history, and a large number of related algorithms have been proposed. An excellent survey of state-of-the-art algorithms is available in [2]. It can be seen from these algorithms that remote sensing image mosaicking generally involves five steps: image registration [14]–[16], extraction of overlapping areas, radiometric normalization [17], [18], seamline detection [19], [20], and image blending [21] (e.g., Laplacian pyramid blending [22] and Poisson image blending [23]). Image registration is the basis of the stitching system. It calculates the consistent geometry of two or more images to align images, which ensures the correctness of the stitching system. Then, the overlapping region is extracted. Remote sensing images are different from ordinary images, some contain geographic information containing geographical coordinates of the images (e.g., GPS data) or onboard position and attitude data (e.g., inertial navigation system data) [24], [25], and some do not. For remote sensing images with geographic reference information, this information can be used to help extract overlapping areas. For remote sensing images without this information, the overlapping areas can be extracted by phase correlation [26] or scale-invariant feature transform (SIFT) [27]. The following steps can reduce artifacts and improve performance. Radiation normalization balances the intensity of image pixels, making their effects appear more subdued. Seamline detection is to pave the way for image blending. It is to find the best seamline locations among the images, and then image blending smoothes the images along this seamline locations.

B. Description of Deformation Model

Image stitching techniques usually use deformation model to globally or locally align images. Early methods used transformations of global parameters, like similarity, affine, and projective transformation. One of the most representative is Autostitch [12]. Autostitch assumes that the images are taken by camera rotation only. Its assumptions limit the use of this method. Generally, the images we obtain are difficult to meet such conditions. People have also made efforts in order to develop a more general model.

Gao *et al.* [28] divided an image scene into two scene planes, a scene into distant and ground planes that sweep out from the camera's location. Then, they used the feature points in the respective scenes to calculate two homography to match the two scene planes respectively. In calculating the homography, a weighted strategy is used to smooth the seamline between the two scene planes. This method is more accurate than using a homography to match the entire image scene, but it is not sufficient for complex scene images. Lin *et al.* [29] introduced a smoothly varying affine field to align the image. The local deformability

and alignment capability are strong and this method can locally adaptively adjust the image, achieve precise local alignment, and maintain global affinity. However, the use of affine regularization is appropriate for interpolation, which may not be optimal for extrapolation, and the affinity is insufficient for completing the perspective transformation [30]. Zaragoza *et al.* [13] proposed as-projective-as-possible deformation model. The purpose of the deformation is to perform a global perspective transformation and allow local nonprojection transformations by sampling the local transformation model for image mosaic. The local model has high degree of freedom and is flexible, which can handle local transformation and reduce ghosting problems. But when the texture in the image becomes lighter and fewer feature points are detected, the method will fail. By segmenting and matching the planar area of the image, Lou *et al.* [31] proposed the piecewise planar region matching approach to achieve more robust image registration. But this approach is not appropriate when the scene areas are more complex. Notice that the nonoverlapping areas in the stitching result will be distorted, shape-preserving half-projective [32] was proposed. This method stitches images by combining homography and similarity transformation, which reduces distortion in nonoverlapping regions in the results. But it cannot handle the parallax of the image, and get a good matching result in the overlapping area. Adaptive as-natural-as-possible also uses global similarity transformation to reduce distortion in nonoverlapping regions. This method linearize the homography in the regions that do not overlap with any other image, and it can adaptively determine angles to correct image shapes efficiently [33]. However, for some complex scene structures, this method cannot accurately match the overlapping regions and thus cause some ghosting in the results. Xiang *et al.* considered that it is difficult to achieve good alignment of images and it is easy to break images structures that are often broken due to insufficient and unreliable point correspondences in stitching low-texture images [34]. Line features are introduced to compute local homography to make matching results more accurate. Li *et al.* [35] proposed a parallax-tolerant image stitching method based on robust elastic warping, which could achieve accurate alignment and efficient processing simultaneously. According to the matching feature points between the images, an analytical warping function is constructed to eliminate the misalignment of the points on the images, and then the images are distorted by the deformation function to achieve a perfect matching result. In addition, the nonrigid deformations have also been considered to stitch images [36]–[38]. However, they are usually difficult to be applied to stitch multiple images due to the error accumulation.

C. Seam Cutting

Noticed that seam cutting [39], [40] is usually a key step for obtaining a perceptually seamless results [35], many related methods have been proposed.

Gao *et al.* [41] proposed a seam-driven image stitching strategy in which the visual quality of the slit is used to guide the transformation estimation. Zhang *et al.* [42] combined the techniques of seam-selection and content-preserving warping to stitch images with large parallax and estimate reasonable seam by considering geometric alignment and image content. A randomized feature selection algorithm is developed to search for hypothesize candidates that may lead to good stitching seams, which combined with content-preserving warping to achieve optimal stitching. Lin *et al.* [43] proposed a seam-guide local alignment approach, in which the final stabilized warp is accomplished through iteratively computing the seam location and the structure-preserving warping. This method can keep the line structure in the image from being distorted during the deformation process. Recently, Lin *et al.* [44] proposed a mesh-based photometric alignment method that combines the superiority of dense photometric alignment with the efficiency of mesh-based deformation, assuming that the corresponding points in the two images follow the brightness constancy constraint. This method minimizes the difference in pixel intensity of the image, instead of minimizing the geometric distance of corresponding feature points. Lin's two methods both emphasize the preservation of the line segment features of the image, which is effective but the computational complexity is higher.

These previous studies all have a certain role in promoting the development of image stitching technology, but they have their own limitations. It is obviously very difficult to develop a general image stitching and obtain a satisfactory result for any input image.

III. Proposed Method

Given a set of UAV images, our task is to combine the images into one large image. In the following, we will provide a detailed presentation of the proposed algorithm. We first describe the project deformation, and proceed to propose multiregion guided local projection deformation to accurately align challenging areas. The overall procedures are illustrated in Fig. 2. As shown in Fig. 2, the images are initially matched by the SIFT feature points, and the correspondence between them is obtained. Then, the target image is meshed and each cell corresponds to a local homography in order to perform the projection transformation. In order to get more accurate local homography, we divide the overlapping regions of input images into multiple regions by classifying feature points. The partitioned regions which serve well scene constraints, are employed to guide the calculation of local homography. Then, we use the obtained series of local homography to perform projection deformation to project the target image onto the reference image. Finally, the image is blended to get the stitching result.

A. Projective Deformation

In the extraction of overlapping areas stage, the SIFT descriptor [45] is used to carry out initial feature matching and obtain the matching relationship of feature points between images.

Given two overlapping images I and $I^{'}$ and their matched points $\mathbf{x}_i = (x_i, y_i)^T$, $\mathbf{y}_i = (x_i^{'}, y_i^{'})^T$, $i = 1, \ldots, N$, the homographic transformation between two images $\mathbf{y} = \mathbf{h}(\mathbf{x})$ can be represented as

$$\mathbf{h}_x(\mathbf{x}) = \frac{h_1 x + h_2 y + h_3}{h_7 x + h_8 y + h_9} \tag{1}$$

$$\mathbf{h}_y(\mathbf{x}) = \frac{h_4 x + h_5 y + h_6}{h_7 x + h_8 y + h_9}. \tag{2}$$

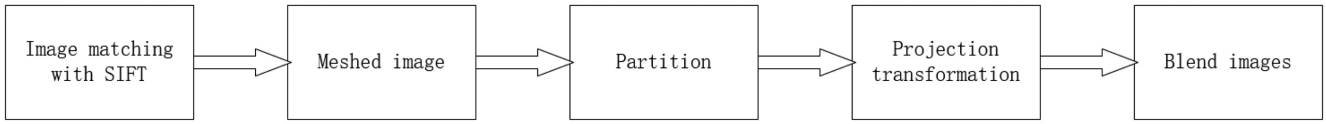

Fig. 2. Flowchart of the proposed methods.

It can be estimated by the relation

$$\widetilde{\mathbf{y}} \sim \mathbf{H}\widetilde{\mathbf{x}} \tag{3}$$

where $\widetilde{\mathbf{x}}$ denotes $\mathbf{x}$ in homogeneous coordinates, $\sim$ indicates the equality up to scale, and $\mathbf{H}$ is the global homography that is a 3×3 matrix. The rows of $\mathbf{H}$ are given by $\mathbf{h}_1 = [h_1\ h_2\ h_3]$, $\mathbf{h}_2 = [h_4\ h_5\ h_6]$, $\mathbf{h}_3 = [h_7\ h_8\ h_9]$. Taking a cross product on both sides of (3), we obtain

$$\mathbf{0}_{3\times 1} = \widetilde{\mathbf{y}} \times \mathbf{H}\widetilde{\mathbf{x}} \tag{4}$$

which can be rewritten as follows:

$$\mathbf{0}_{3\times 1} = \begin{bmatrix} \mathbf{0_{1\times 3}} & -\tilde{\mathbf{x}}^T & y^{'}\tilde{\mathbf{x}}^T \\ \tilde{\mathbf{x}}^T & \mathbf{0}_{1\times 3} & -x^{'}\tilde{\mathbf{x}}^T \\ -y^{'}\tilde{\mathbf{x}}^T & x^{'}\tilde{\mathbf{x}}^T & \mathbf{0}_{1\times 3} \end{bmatrix} \mathbf{h}, \mathbf{h} = \begin{bmatrix} \mathbf{h_1^T} \\ \mathbf{h}_2^T \\ \mathbf{h}_3^T \end{bmatrix}. \tag{5}$$

Only two of the rows are linearly independent and we will denote the 9×1 vector in (5) as $\mathbf{h}$.

Direct linear transformation [46] is the framework for estimating $\mathbf{H}$ from a set of matching points containing outliers. We vectorize $\mathbf{H}$ into a vector $\mathbf{h}$ and $\mathbf{a}_i$ represent first-two rows of the LHS matrix in (5) computed for the ith point match $\{\mathbf{x}_i, \mathbf{y}_i\}$. The quantity $\|\mathbf{a}_i\mathbf{h}\|$ is the algebraic error and the sum of squared algebraic errors is minimized

$$\hat{\mathbf{h}} = \arg\min_{\mathbf{h}} \sum_{i=1}^{N} \|\mathbf{a}_i\mathbf{h}\|^2. \tag{6}$$

By stacking vertically $\mathbf{a}_i$ for all i into matrix $\mathbf{A}$ of size $2N \times 9$, the problem can be rewritten as

$$\hat{\mathbf{h}} = \arg\min_{\mathbf{h}} \sum_{i=1}^{N} \|\mathbf{A}\mathbf{h}\|^2. \tag{7}$$

The solution is the least significant right singular vector of $\mathbf{A}$. Given the estimated $\mathbf{H}$ (reconstructed from $\hat{\mathbf{h}}$), to align the images, an arbitrary pixel $\mathbf{x}_*$ in the source image I is projected to the pixel $\mathbf{y}_*$ in the target image $I^{'}$ by

$$\widetilde{\mathbf{y}}_* \sim \mathbf{H}\widetilde{\mathbf{x}}_*. \tag{8}$$

B. Multiregion Guided Local Projective Deformation

For UAV images, the view I and $I^{'}$ do not differ purely by rotation or are not of a planar scene, using a global homography inevitably yields ghosting effects in the alignment. In this case, we mesh the image and uniformly partition the image into a grid of 100×100 cells, and each cell with a local response. We introduce a local homography

$$\widetilde{\mathbf{y}}_* \sim \mathbf{H}_*\widetilde{\mathbf{x}}_*. \tag{9}$$

Each pixel $\mathbf{x}_*$ corresponds to a location dependent homography $\mathbf{H}_*$, where $\mathbf{x}_*$ is estimated from the weighted problem

$$\mathbf{h}_* = \arg\min_{\mathbf{h}} \sum_{i=1}^{N} \|w_*^i\mathbf{a}_i\mathbf{h}\|^2. \tag{10}$$

The scalar weights $\{w_*^i\}_{i=1}^N$ are the weight of each feature point in the overlapping region.

By considering the characteristics of UAV image, we propose a strategy to calculate the scalar weights $\{w_*^i\}_{i=1}^N$. We divide the overlapping region into some small regions and multiple regions have different weights. The region where the pixel $\mathbf{x}_*$ is located give higher importance. For feature points in one region, the point that are closer to $\mathbf{x}_*$ give higher importance. There are some limitations if we define the weights of all SIFT feature points according to the geometric distance to pixel $\mathbf{x}_*$. Especially for cell at the boundaries of different surfaces of buildings, the projection model inside must be different.

We use a simple method to divide the overlapping region into some small regions. After obtaining the feature point matches, we first remove the outliers using RANSAC [47] with threshold ε_g. This value can be set slightly larger so that there are as many matching points as possible in the overlapping area of the two images. Then, we use RANSAC with a threshold ε_l, where $\varepsilon_l < \varepsilon_g$, and we remove the inliers. So we can get a smaller set of match points from the inliers, and the points of the small set is defined as G_1. This is repeated until the number of inliers is small than κ. In this way, all the feature points are divided into some groups $G_1, G_2, \ldots G_n$ and each group corresponds to a region. We can define the scalar weights $G_j(w_*^i)$ as

$$G_j(w_*^i) = \exp(-\|\mathbf{x}_* - \mathbf{x}_i\|^2/\delta^2) \tag{11}$$

where δ is a scale parameter. G_j is jth group and $\mathbf{x}_i$ is ith point match in the G_j. We can define the scalar weights $\{w_*^i\}_{i=1}^N$ as

$$w_*^i = \frac{l_{\text{out}}}{l_{\text{in}} + l_{\text{out}}} G_{\text{in}}(w_*^i) + \frac{l_{\text{in}}}{l_{\text{in}} + l_{\text{out}}} G_{\text{out}}(w_*^i) \tag{12}$$

where G_{in} means $\mathbf{x}_*$ is in the region corresponding to G_{in} and G_{out} means $\mathbf{x}_*$ is not in the region corresponding to G_{in}. l_{in} and l_{out} are the distances from $\mathbf{x}_*$ to the closest feature points in and out of the group G_{in}.

The problem (10) can be written in the matrix form

$$\mathbf{h}_* = \arg\min_{\mathbf{h}} \sum_{i=1}^{N} \|\mathbf{W}_*\mathbf{A}\mathbf{h}\|^2 \tag{13}$$

where the weight matrix $\mathbf{W}_*$ of size $2N \times 2N$ is composed as $\mathbf{W}_* = \text{diag}([w_*^1\ w_*^1\ w_*^2\ w_*^2\ \ldots w_*^N\ w_*^N])$. This is a weighted SVD (WSVD) problem, and the solution is simply the least significant right singular vector of $\mathbf{W}_*\mathbf{A}$.

Algorithm 1: multi-region local projection deformation.

Input: Images I , $I^{'}$ with overlops and their matched points $\mathbf{x}_i = (x_i, y_i)^T$, $\mathbf{y}_i = (x_i^{'}, y_i^{'})^T$, $i = 1, \ldots, N$;
Output: Result of mosaicing;
Project keypoints from $I^{'}$ onto I and match;
Mesh reference image $I^{'}$;
for *each cell in* $I^{'}$ **do**
  Calculate weights for current cell center $\mathbf{x}_*$;
  for *i = 1, ..., N* **do**
    Computer local homography by(13);
  end
  Using local homography, composite pixels in current cell;
end

Since there are only feature points in the overlapping area of the two images, problem (13) may be unstable when $\mathbf{x}_*$ is in the nonoverlapping area of the two images and many of the weights are insignificant. To avoid this problem, we offset the weights with a small value γ within 0 and 1

$$w_*^i = \max\left(\frac{l_{\text{out}}}{l_{\text{in}} + l_{\text{out}}} G_{\text{in}}(w_*^i) + \frac{l_{\text{in}}}{l_{\text{in}} + l_{\text{out}}} G_{\text{out}}(w_*^i), \gamma\right). \tag{14}$$

This also serves to regularize the warp and minimizes the distortion in the image. Algorithm 1 summarizes our method.

C. Multiple Image Stitching

Given a set of overlapping images $\{I^k\}_{k=1}^K$, we aim to stitch these images into a panoramic image. Each image has more than one image with overlapping areas, and errors are inevitably accumulated when integrated together. In order to reduce the accumulated errors, we must adjust these errors as a whole. The initial step is to find reference image I^R from input images as common surface. We apply the keypoint-based panorama recognition method [12].

For an arbitrary location $\mathbf{x}_*$ in I^R, we have a set of location-dependent homographies $\{\mathbf{H}_*^k\}_{k=1}^K$, where each $\mathbf{H}_*^k$ maps $\mathbf{x}_*$ from I^R to I^k. Considering the cumulative error during image mosaic, we minimize the cost to minimize the transfer error of all correspondences

$$E_*(\Theta) = \sum_{i=1}^{N} \frac{w_*^i}{\sum_{k=1}^K \xi_{ik}} \sum_{k=1}^{K} \xi_{ik} \|\mathbf{x}_i^k - f(\mathbf{p}_i, \mathbf{H}_*^k)\|^2 \tag{15}$$

where $\Theta = [\mathbf{H}_1^k, \ldots, \mathbf{H}_*^k, \mathbf{p}_1, \ldots, \mathbf{p}_N]$ and $f(\mathbf{p}, \mathbf{H})$ is the project warp defined as

$$f(\mathbf{p}, \mathbf{H}) = \left[\frac{\mathbf{h}_1[\mathbf{p}^T 1]^T}{\mathbf{h}_3[\mathbf{p}^T 1]^T} \; \frac{\mathbf{h}_2[\mathbf{p}^T 1]^T}{\mathbf{h}_3[\mathbf{p}^T 1]^T}\right]^T. \tag{16}$$

We introduce a parameter $\xi_{ik} \in \{0, 1\}$, where $\xi_{ik} = 1$ indicates that correspondence exists; otherwise, $\xi_{ik} = 0$. Algorithm 2 summarizes multiple image stitching.

Algorithm 2: Multiple image stitching based on region-based local projective warp.

Input: Input images $\{I^k\}_{k=1}^K$ with overlaps;
Output: Panorama creation;
Choose reference image I^R from $\{I^k\}_{k=1}^K$ as common surface;
Project all keypoints from $\{I^k\}_{k=1}^K$ onto I^R;
Register points in I^R with points in $\{I^k\}_{k=1}^K$;
Mesh the image I^R;
for *each cell in* I^R **do**
  Calculate weights for current cell center $\mathbf{x}_*$ by (14);
  for *k = 1, ..., K* **do**
    Yield homography $\mathbf{H}_*^k$ by (13);
  end
  Update all $\{\mathbf{H}_*^k\}_{k=1}^K$ by (15);
  Using $\{\mathbf{H}_*^k\}_{k=1}^K$, composite pixels in current cell;
end

IV. Experimental Results

A group of experiments are carried out to evaluate performance of our method. These included 1) comparison of global homography and local warp; 2) performance comparison of multiregion guided local deformation and existing methods; 3) multiple image stitching. In our experiments, the images used in the experiment were collected by the feimaD200 equipped with SONY ILCE600. The first set of images including Figs. 4 and 9 were collected in Pengjiapo Village, Guizhou Town, Zigui County, Yichang City, and the other set of images including Figs. 5–7 were collected at China University of Geosciences, Wuhan, China. The corresponding points are detected and matched using SIFT and the same matching data is applied in all the tested methods. In order to compare these methods more clearly, we do not add some postprocessing like seam cutting and simply blend the aligned images by intensity averaging such that any misalignments remain obvious. The parameter settings for the compared methods follow the recommendations of their corresponding papers. For our method, we set δ as 12, γ as 0.01, the threshold ε_g as 0.1, the threshold ε_l as 0.001, and the threshold for inlier number κ as 50.

A. Comparison of Global Homography and Local Warp

The UAV images may not be on a plane, yielding parallax on the images. In the projection transformations of matching images, Autostitch (Baseline) completes the transformation by using a global homography, which produces some bad effects (misalignment artifacts or ghosting) caused by image parallax. We apply local projective warp to match UAV images to reduce bad effects in the results compared with global homography.

We use an example in Fig. 3 to illustrate the difference between global homography and local warp when matching images. In Fig. 3, these points are the matching points on the two images. Because the image has parallax, the distribution of the matching points is not uniform. When a global homography is used for deformation, it is unable to model the local deviations

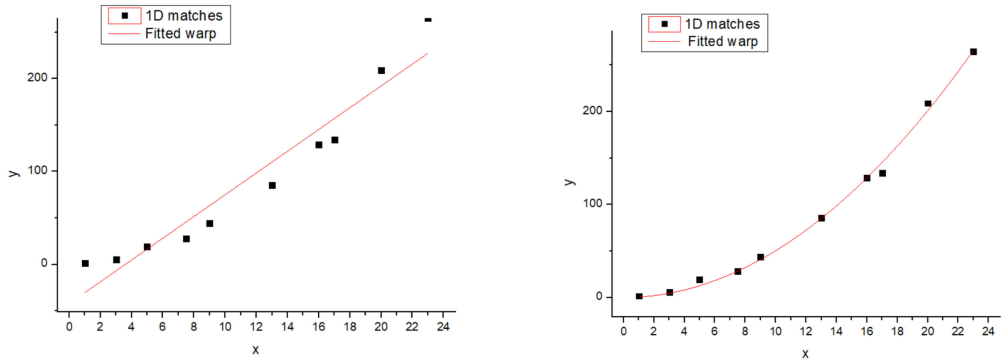

Fig. 3. To generate a 1-D analogy of image stitching, a set of 1-D matches $\{\mathbf{x}_i, \mathbf{y}_i\}_{i=1}^{N}$ are generated by projecting a 2D point cloud onto two 1D image "planes". Here, there is a parallax between the two images. The first indicates that the match points are warped by a global homography and the second indicates that the match points are warped by some local homography.

Fig. 4. Mosaic results. The first row is the two images to be stitched together. The second and third rows are two stitched images by global homography and local wrap, respectively. The ghostly parts are highlighted in red boxes and correspond to each other next to the results.

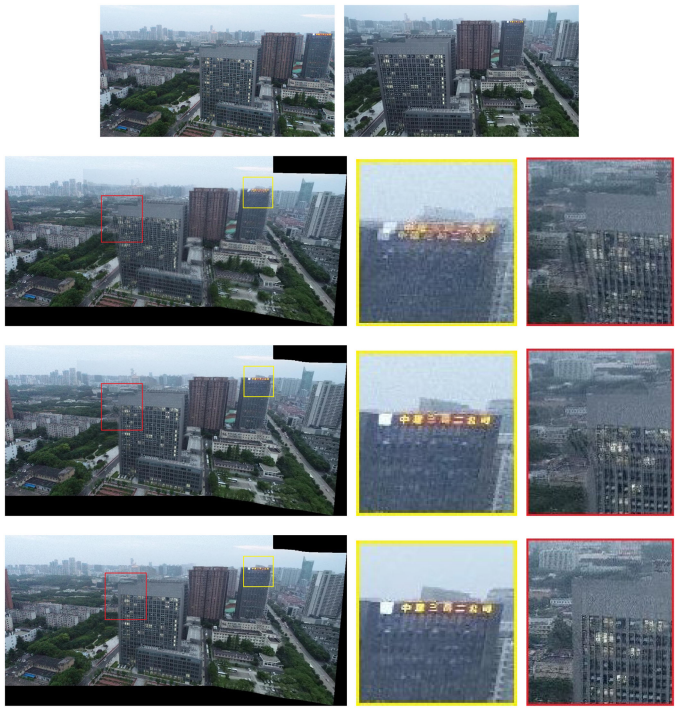

Fig. 5. Mosaic results. The first row is the two images to be stitched. The second, third, and fourth rows are the stitching results of global homography, local warp, and our method, respectively. The ghostly parts are highlighted in yellow and red boxes and correspond to each other next to the results.

of the data and cannot contain all matching points because it is a rigid transformation. Instead, local warp can interpolate the local deviations flexibly, so it can contain as many matching points as possible. We also perform the experiment, and Fig. 4 shows the results. In Fig. 4, the first row is the two images to be stitched together. The second and third rows, respectively, present the results of global homography and local warp. In addition, two representative areas of result are highlighted. In the second row, strictly aligning these images through global homography is difficult and the ground lines in the red boxes are clearly wrong. In the third row, the result of our method is natural and free of ghosts. The line in the red box is complete, because local warp can match the objects in the overlapping regions efficiently compared to global homography.

B. Multiregion Guided Local Projective Deformation

UAV remote sensing is a low-altitude technology, and there may be some tall buildings in the image. Fig. 5 shows a challenging case of an urban scenario, which shows a comparison of global homography, local warp and our method. The first row is the images to be stitched together. The results of different methods are presented by rows and two representative areas of each resulting image are highlighted. As the baseline of

Fig. 6. Mosaic results on Fig. 1. Rows 1 to 6 are the stitching results of Autostitch, APAP, AANAP, SPHP, REW, and our method, respectively. The ghostly parts are highlighted in red, yellow, and blue boxes and correspond to each other next to the results.

comparison, the second row shows the results of global homography and significant artifacts appear in highlighted areas due to the limitation of a global homography. In particular, the parallax of the two images is too large for high building targets. Misalignments are evident in the image alignment phase, which directly leads to artifacts. The third row shows the results of local warp. Because of the multiple local matrices, the matching capability becomes stronger, which can handle some areas of small parallax. For example, some short buildings are well aligned, but tall buildings still have challenges. The last row

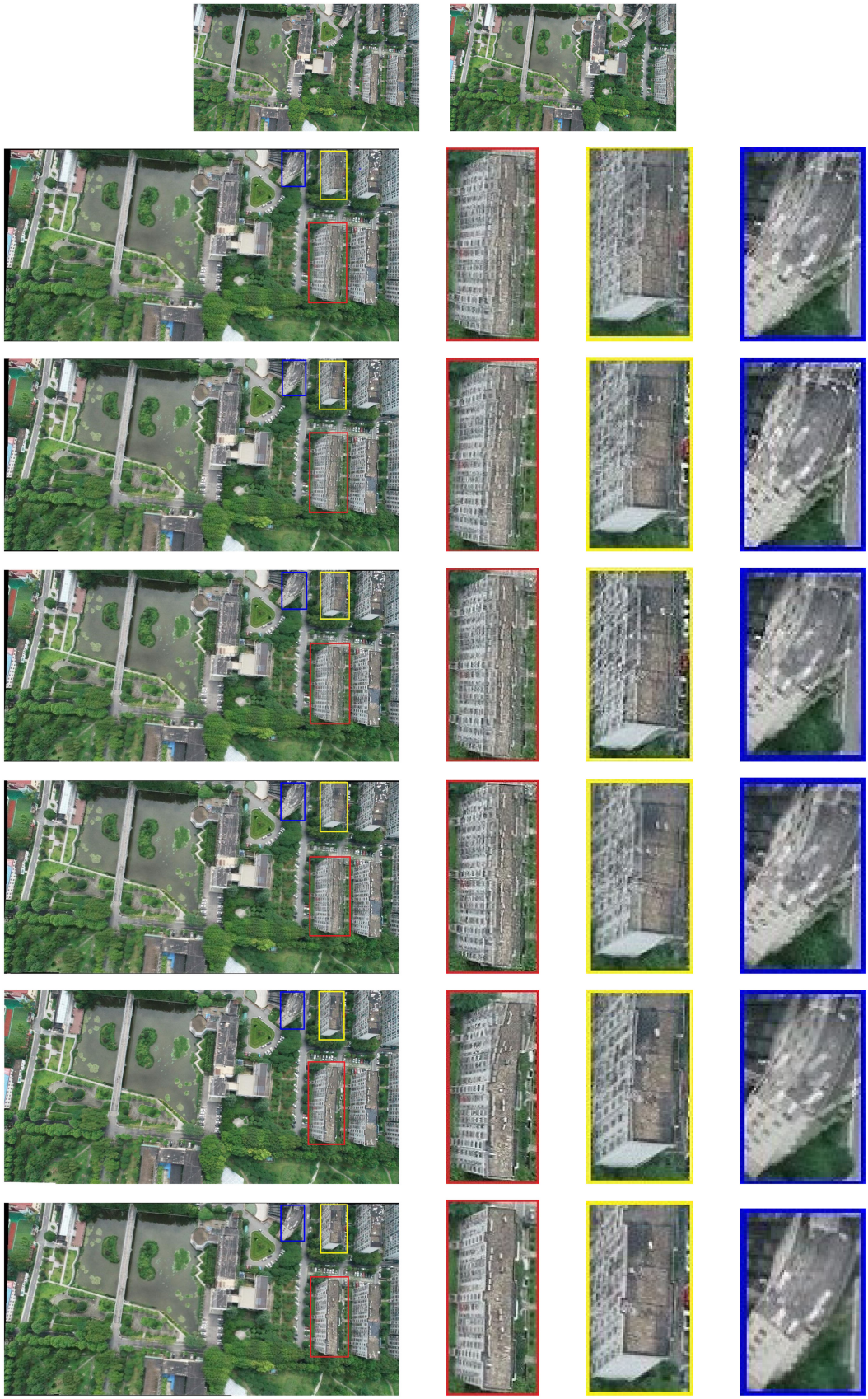

Fig. 7. Mosaic results. The first row is the two images to be stitched. Rows 2 to 7 are the stitching results of Autostitch, APAP, AANAP, SPHP, REW, and our method, respectively. The ghostly parts are highlighted in red, yellow, and blue boxes and correspond to each other next to the results.

shows the results of our method. Since region-based local warp in our model performs well, our method can overcome this challenge and obtain better results.

In addition, we compare our method with some image mosaic algorithms, namely, Autostitch [12], APAP [13], SPHP [32], AANAP [33], and REW [35]. Some experiments are carried out to evaluate the performance of our method, and two representative sets of experimental results are presented here. Figs. 6 and 7 show the images obtained in two different scenes.

In Fig. 6, two images to be stitched are in Fig. 1 and rows 1 to 6, respectively, present the results of various methods and three representative areas of each resulting image are highlighted. The first row is the results of Autostitch. Autostitch is the method based on global homography. As shown, due to the model deficiencies, the baseline warp cannot provide satisfactory stitching results. The second row is the result of APAP. APAP is the method based on local warp, which can alleviate these ghosts. The third and fourth rows are the results of AANAP and SPHP. AANAP introduces similar local adaptive transformations in the overlapping regions to achieve better stitching quality, but misalignments are evident in high building areas. SPHP also cannot address the challenge. The fifth and sixth rows are the results of REW and our method. REW improve the stitching performance but there are still artifacts. Our methods can address this challenge and acquire better results than these methods. In Fig. 7, the first row is the two images to be stitched. Rows 2 to 7, respectively, present the results of Autostitch, APAP, SPHP, AANAP, REW, and our method. Comparing these results, Autostitch is the baseline of comparison and significant artifacts appear in highlighted areas. Other advanced methods can almost alleviate artifacts, but the result of these methods contain evident artifacts in high building areas. Instead, our method is more suitable.

To quantify the alignment accuracy of different mosaics, root mean squared error (RMSE), mean absolute error (MAE), and the metrics of correlation (Cor) [34] are adopted. RMSE is given as follows:

$$\mathrm{RMSE}(I, I^{'}) = \sqrt{\frac{1}{N}\sum\nolimits_{i=1}^{N}(\mathbf{h}_*(\mathbf{x}_i) - \mathbf{y}_i)^2} \tag{17}$$

where $\mathbf{x}_i$ and $\mathbf{y}_i$ are keypoint matches $\{\mathbf{x}_i, \mathbf{y}_i\}_i^N$, $i = 1, \ldots N$ in images I and $I^{'}$, $\mathbf{h}_*(\mathbf{x}_i)$ is the projection of $\mathbf{x}_i$ onto $I^{'}$ by local homography. The smaller the index value is, the better the result is. MAE is defined as follows:

$$\mathrm{MAE}(I, I^{'}) = \frac{1}{N}\sum_{i=1}^{N}|\mathbf{h}_*(\mathbf{x}_i) - \mathbf{y}_i|. \tag{18}$$

The smaller the index value is, the better the result is. Cor is defined as one minus the normalized cross correlation (NCC) over the neighborhood of a 3×3 window, that is

$$\mathrm{Cor}(I, I^{'}) = \sqrt{\frac{1}{N}\sum\nolimits_{i=1}^{N}(1 - \mathrm{NCC}(\mathbf{x}_i, \mathbf{y}_i))^2}. \tag{19}$$

Cor reflects the dissimilarity of two images in the overlapping regions. The smaller the Cor value is, the better the stitching result is.

TABLE I
COMPARISON OF RMSE

	Fig. 4	Fig. 5	Fig. 6	Fig. 7
Autostitch [12]	10.51	16.46	20.44	15.15
APAP [13]	5.74	11.42	14.56	9.51
AANAP [33]	4.97	10.24	12.40	7.86
SPHP [32]	9.51	14.91	18.25	13.96
REW [35]	4.65	8.62	10.85	7.40
Ours	5.10	4.34	8.15	5.65

TABLE II
COMPARISON OF COMPUTATIONAL COST

	image size	APAP [13]	AANAP [33]	Ours
Fig. 4	1024×682	8.85	12.10	12.78
Fig. 5	1024×576	7.24	9.34	10.11
Fig. 6	1024×682	8.42	11.38	12.19
Fig. 7	800×450	4.36	6.57	7.39

Table I shows the result of RMSE. We compute the RMSE for the compared methods in Figs. 6 and 7 and the results are also shown in this article. In addition, we also compute the RMSE for the various methods in Figs. 4 and 5, comparing them together. In Table I, Autostitch has the highest value because it is the worst for image alignment. RMSE of other methods is smaller. In addition, for Fig. 4, our method does not show much advantage here, because there are basically no tall buildings in the overlapping area of the two images. However, for Figs. 5–7, there are more tall buildings in the image, and our method achieves the best quantitative results. We also compute MAE and Cor for the various methods in Figs. 4–7. In order to better reflect the advantages of our method, we made the experimental data into a statistical graph. The experimental results are depicted by curves in Fig. 8. The first is the result of MAE. Our method always has the smallest value, except that the value of REW in Fig. 4 is smaller than ours. The second is the result of Cor and it can be easily seen that our method outperforms all the compared methods.

In order to evaluate the time efficiency of our method, we compare it with some local adaptive stitching methods, namely APAP and AANAP. We do not compare with global projection deformation. The computational cost of Autostitch is definitely much smaller than the local projection deformation, because it only needs to calculate a homography, and the local warp needs to calculate a series of homography. The test data set includes several data in this article. Table II shows the result of computational cost. It can be seen from Table II that our computational cost is basically consistent with several other local deformation methods.

C. Multiple Image Stitching

The panorama examples in Fig. 9 demonstrate the performance of our proposed method with multiple images. We compare our method with Autostitch (Baseline). In Fig. 9, the first row is input images and the second row are, respectively, generated using the global homography and our method. Four

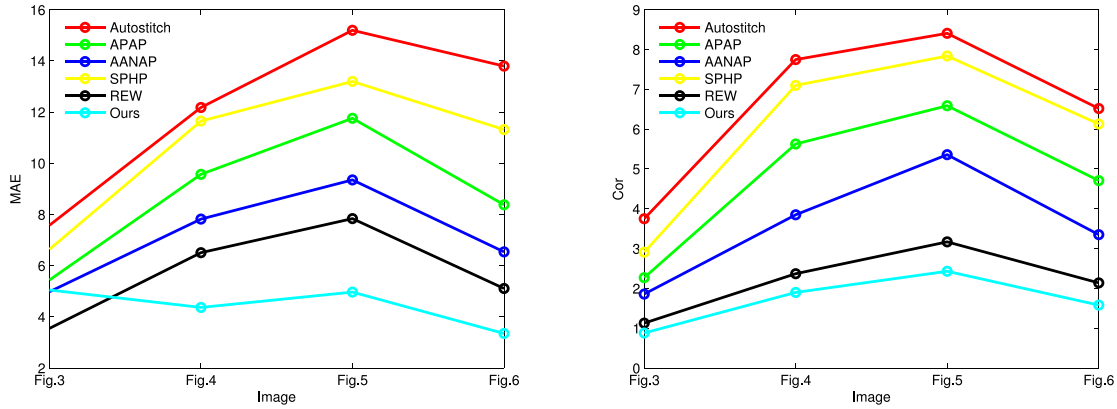

Fig. 8. Comparison of MAE and Cor in Figs. 4–7. Different methods are represented by different colored polylines.

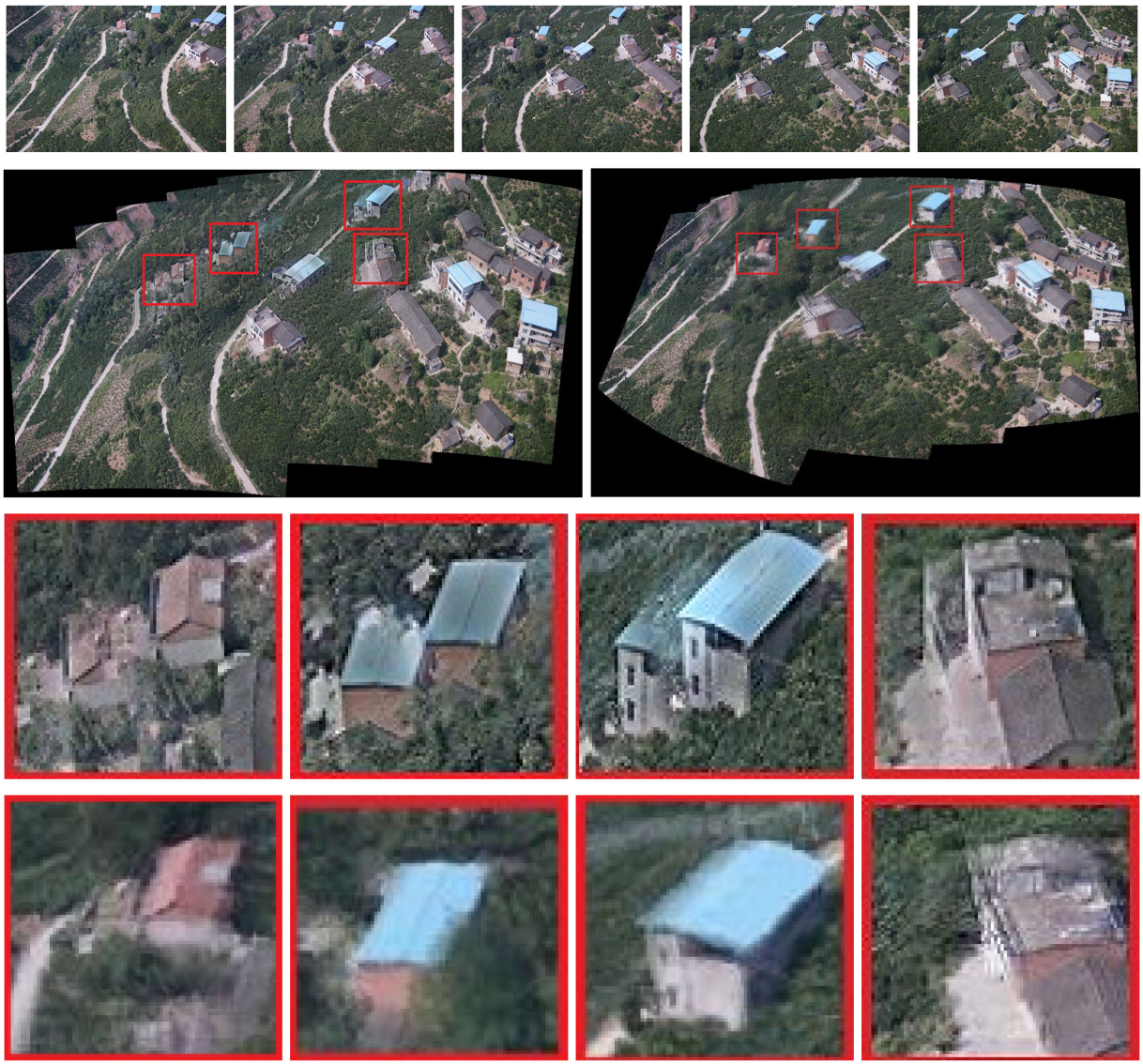

Fig. 9. Experimental results of stitching multiple images. The first row is the image to be stitched together. The second row is the results of Autostitch and ours method, respectively. Red boxes highlight the ghostly parts.

representative areas are highlighted to show the alignment quality in detail. The third and fourth rows are highlighted areas of Autostitch and our method, respectively. Results show that our stitching system has a better effect than Autostitch, and the ghosting effect is considerably reduced in some building areas. In Autostitch, there are some alignment errors when two images are stitched. When multiple images are stitched, the alignment errors are propagated and amplified and Autostitch cannot efficiently remove the accumulated error. By contrast, noticeable alignment errors are not introduced in our method and our results show much fewer artifacts than Autostitch.

V. Conclusion

In this article, we propose a novel UAV image mosaic method based on multiregion guided local projection deformation. The image is initially meshed and each cell corresponds to a local homography for the alignment. Then, based on RANSAC, the overlapping regions of two images are divided into multiple regions by classifying feature points. A proposed strategy where multiple regions have different weights is used to calculate local homography accurately. The proposed method achieves a better alignment in overlapping regions and can address the challenges mentioned. It is more suitable for UAV images and our experimental results show our advantages. Our image stitching method can be used in many fields, such as remote sensing image processing, urban reconstruction after the disaster, environmental monitoring, etc. However, our method sacrifices the stiffness of the stitching image. The effect is good when stitching two images, but distortion is observed in the result when stitching multiple images. Our future work will concentrate on this topic.

References

[1] C. Liu, S. Zhang, and A. Akbar, "Ground feature oriented path planning for unmanned aerial vehicle mapping," *IEEE J. Sel. Topics Appl. Earth Observ. Remote Sens.*, vol. 12, no. 4, pp. 1175–1187, Apr. 2019.

[2] X. Li, R. Feng, X. Guan, H. Shen, and L. Zhang, "Remote sensing image mosaicking: Achievements and challenges," *IEEE Geosci. Remote Sens. Mag.*, vol. 7, no. 4, pp. 8–22, Dec. 2019.

[3] J. Ma, X. Jiang, J. Jiang, J. Zhao, and X. Guo, "LMR: Learning a two-class classifier for mismatch removal," *IEEE Trans. Image Process.*, vol. 28, no. 8, pp. 4045–4059, Aug. 2019.

[4] J. Chen, Q. Wan, L. Luo, Y. Wang, and D. Luo, "Drone image stitching based on compactly supported radial basis function," *IEEE J. Sel. Topics Appl. Earth Observ. Remote Sens.*, vol. 12, no. 11, pp. 4634–4643, Nov. 2019.

[5] E. Adel, M. Elmogy, and H. Elbakry, "Image stitching based on feature extraction techniques: A survey," *Int. J. Comput. Appl.*, vol. 99, no. 6, pp. 1–8, 2014.

[6] B. Ye, Z. Cai, T. Lan, and W. Cao, "A novel stitching method for dust and rock analysis based on YUTU rover panoramic imagery," *IEEE J. Sel. Topics Appl. Earth Observ. Remote Sens.*, vol. 12, no. 11, pp. 4457–4466, Nov. 2019.

[7] X. Li, N. Hui, H. Shen, Y. Fu, and L. Zhang, "A robust mosaicking procedure for high spatial resolution remote sensing images," *ISPRS J. Photogrammetry Remote Sens.*, vol. 109, pp. 108–125, 2015.

[8] D. V. Fedorov, L. M. G. Fonseca, C. Kenney, and B. S. Manjunath, "Automatic registration and mosaicking system for remotely sensed imagery," in *Proc. Image Signal Process. Remote Sens. VIII*, 2003, vol. 4885, pp. 444–451.

[9] D. Turner, A. Lucieer, and C. Watson, "An automated technique for generating georectified mosaics from ultra-high resolution unmanned aerial vehicle (UAV) imagery, based on structure from motion (SFM) point clouds," *Remote Sens.*, vol. 4, no. 5, pp. 1392–1410, 2012.

[10] G. De Grandi, J.-P. Malingreau, and M. Leysen, "The ERS-1 central Africa mosaic: A new perspective in radar remote sensing for the global monitoring of vegetation," *IEEE Trans. Geosci. Remote Sens.*, vol. 37, no. 3, pp. 1730–1746, May 1999.

[11] J. Zaragoza, T.-J. Chin, M. S. Brown, and D. Suter, "As-projective-as-possible image stitching with moving DLT," *IEEE Trans. Pattern Anal. Mach. Intell.*, vol. 36, no. 7, pp. 1285–1298, Jul. 2014.

[12] M. Brown and D. G. Lowe, "Automatic panoramic image stitching using invariant features," *Int. J. Comput. Vision*, vol. 74, no. 1, pp. 59–73, 2007.

[13] J. Zaragoza, T.-J. Chin, M. S. Brown, and D. Suter, "As-projective-as-possible image stitching with moving DLT," in *Proc. IEEE Conf. Comput. Vision Pattern Recognit.*, 2013, pp. 2339–2346.

[14] J. Ma, J. Zhao, J. Jiang, H. Zhou, and X. Guo, "Locality preserving matching," *Int. J. Comput. Vision*, vol. 127, no. 5, pp. 512–531, 2019.

[15] J. Ma, J. Jiang, H. Zhou, J. Zhao, and X. Guo, "Guided locality preserving feature matching for remote sensing image registration," *IEEE Trans. Geosci. Remote Sens.*, vol. 56, no. 8, pp. 4435–4447, Aug. 2018.

[16] Q. Guo, M. He, and A. Li, "High-resolution remote-sensing image registration based on angle matching of edge point features," *IEEE J. Sel. Topics Appl. Earth Observ. Remote Sens.*, vol. 11, no. 8, pp. 2881–2895, Aug. 2018.

[17] C. Zhong, Q. Xu, and B. Li, "Relative radiometric normalization for multitemporal remote sensing images by hierarchical regression," *IEEE Geosci. Remote Sens. Lett.*, vol. 13, no. 2, pp. 217–221, Feb. 2016.

[18] Q. Du, N. Raksuntorn, A. Orduyilmaz, and L. M. Bruce, "Automatic registration and mosaicking for airborne multispectral image sequences," *Photogrammetric Eng. Remote Sens.*, vol. 74, no. 2, pp. 169–181, 2008.

[19] W. Zhang, B. Guo, M. Li, X. Liao, and W. Li, "Improved seam-line searching algorithm for UAV image mosaic with optical flow," *Sensors*, vol. 18, no. 4, 2018, Art. no. 1214.

[20] L. Li, J. Yao, R. Xie, and J. Li, "Edge-enhanced optimal seamline detection for orthoimage mosaicking," *IEEE Geosci. Remote Sens. Lett.*, vol. 15, no. 5, pp. 764–768, May 2018.

[21] R. T. Whitaker, "A level-set approach to image blending," *IEEE Trans. Image Process.*, vol. 9, no. 11, pp. 1849–1861, Nov. 2000.

[22] P. J. Burt and E. H. Adelson, "A multiresolution spline with application to image mosaics," *ACM Trans. Graph.*, vol. 2, no. 4, pp. 217–236, 1983.

[23] P. Pérez, M. Gangnet, and A. Blake, "Poisson image editing," *ACM Trans. Graph.*, vol. 22, no. 3, pp. 313–318, 2003.

[24] T. Suzuki, Y. Amano, and T. Hashizume, "Vision based localization of a small UAV for generating a large mosaic image," in *Proc. SICE Annu. Conf.*, 2010, pp. 2960–2964.

[25] J. Shi, J. Wang, and Y. Xu, "Use of GPS/INS observations for efficient matching of UAV images," in *Proc. Int. Global Navigation Satell. Syst. Soc. IGNSS Symp.*, 2011.

[26] D.-H. Kim, Y.-I. Yoon, and J.-S. Choi, "An efficient method to build panoramic image mosaics," *Pattern Recognit. Lett.*, vol. 24, no. 14, pp. 2421–2429, 2003.

[27] Z. Hua, Y. Li, and J. Li, "Image stitch algorithm based on SIFT and MVSC," in *Proc. 7th Int. Conf. Fuzzy Syst. Knowl. Discovery*, 2010, vol. 6, pp. 2628–2632.

[28] J. Gao, S. J. Kim, and M. S. Brown, "Constructing image panoramas using dual-homography warping," in *Proc. CVPR*, 2011, pp. 49–56.

[29] W.-Y. Lin, S. Liu, Y. Matsushita, T.-T. Ng, and L.-F. Cheong, "Smoothly varying affine stitching," in *Proc. CVPR*, 2011, pp. 345–352.

[30] J. Chen, Q. Xu, L. Luo, Y. Wang, and S. Wang, "A robust method for automatic panoramic UAV image mosaic," *Sensors*, vol. 19, no. 8, 2019, Art. no. 1898.

[31] Z. Lou and T. Gevers, "Image alignment by piecewise planar region matching," *IEEE Trans. Multimedia*, vol. 16, no. 7, pp. 2052–2061, Nov. 2014.

[32] C.-H. Chang, Y. Sato, and Y.-Y. Chuang, "Shape-preserving half-projective warps for image stitching," in *Proc. IEEE Conf. Comput. Vision Pattern Recognit.*, 2014, pp. 3254–3261.

[33] C.-C. Lin, S. U. Pankanti, K. N. Ramamurthy, and A. Y. Aravkin, "Adaptive as-natural-as-possible image stitching," in *Proc. IEEE Conf. Comput. Vision Pattern Recognit.*, 2015, pp. 1155–1163.

[34] T.-Z. Xiang, G.-S. Xia, X. Bai, and L. Zhang, "Image stitching by line-guided local warping with global similarity constraint," *Pattern Recognit.*, vol. 83, pp. 481–497, 2018.

[35] J. Li, Z. Wang, S. Lai, Y. Zhai, and M. Zhang, "Parallax-tolerant image stitching based on robust elastic warping," *IEEE Trans. Multimedia*, vol. 20, no. 7, pp. 1672–1687, Jul. 2018.

[36] J. Ma, H. Zhou, J. Zhao, Y. Gao, J. Jiang, and J. Tian, "Robust feature matching for remote sensing image registration via locally linear transforming," *IEEE Trans. Geosci. Remote Sens.*, vol. 53, no. 12, pp. 6469–6481, Dec. 2015.
[37] J. Ma, J. Wu, J. Zhao, J. Jiang, H. Zhou, and Q. Z. Sheng, "Nonrigid point set registration with robust transformation learning under manifold regularization," *IEEE Trans. Neural Netw. Learn. Syst.*, vol. 30, no. 12, pp. 3584–3597, Dec. 2019.
[38] J. Ma, W. Qiu, J. Zhao, Y. Ma, A. L. Yuille, and Z. Tu, "Robust l_2e estimation of transformation for non-rigid registration," *IEEE Trans. Signal Process.*, vol. 63, no. 5, pp. 1115–1129, Mar. 2015.
[39] A. Agarwala *et al.*, "Interactive digital photomontage," *ACM Trans. Graph.*, vol. 23, no. 3, pp. 294–302, 2004.
[40] A. Eden, M. Uyttendaele, and R. Szeliski, "Seamless image stitching of scenes with large motions and exposure differences," in *Proc. IEEE Conf. Comput. Vision Pattern Recognit.*, vol. 2, 2006, pp. 2498–2505.
[41] J. Gao, Y. Li, T.-J. Chin, and M. S. Brown, "Seam-driven image stitching," in *Proc. Eurographics (Short Papers)*, 2013, pp. 45–48.
[42] F. Zhang and F. Liu, "Parallax-tolerant image stitching," in *Proc. IEEE Conf. Comput. Vision Pattern Recognit.*, 2014, pp. 3262–3269.
[43] K. Lin, N. Jiang, L.-F. Cheong, M. Do, and J. Lu, "SEAGULL: Seam-guided local alignment for parallax-tolerant image stitching," in *Proc. Eur. Conf. Comput. Vision*, 2016, pp. 370–385.
[44] K. Lin, N. Jiang, S. Liu, L.-F. Cheong, M. Do, and J. Lu, "Direct photometric alignment by mesh deformation," in *Proc. IEEE Conf. Comput. Vision Pattern Recognit.*, 2017, pp. 2405–2413.
[45] D. G. Lowe, "Distinctive image features from scale-invariant keypoints," *Int. J. Comput. Vision*, vol. 60, no. 2, pp. 91–110, 2004.
[46] Z. Zhang, "Parameter estimation techniques: A tutorial with application to conic fitting," *Image Vision Comput.*, vol. 15, no. 1, pp. 59–76, 1997.
[47] M. A. Fischler and R. C. Bolles, "Random sample consensus: A paradigm for model fitting with applications to image analysis and automated cartography," in *Proc. Readings Comput. Vision*, 1987, pp. 726–740.

Quan Xu was born in Jingzhou, China, in 1995. He received the B.S. degree from the School of Electronic Information, Yangtze University, Jingzhou, China, in 2018. He is currently working toward the M.S. degree with the School of Mechanical Electronic and Electronic Information, China University of Geosciences, Wuhan, China.

His research interests include computer vision and pattern recognition.

Jun Chen received the B.S. degree in electronic and information engineering and the M.S. degree in communication and information system from the China University of Geosciences, Wuhan, China, in 2002 and 2004, respectively, and the Ph.D. degree in communication and information system from the Huazhong University of Technology, Wuhan, China, in 2014.

From 2004 to 2008, she was an Assistant Professor with the China University of Geosciences, where she is currently an Associate Professor with the School of Automation. Her research interests include computer vision and pattern recognition, geoscience, and remote sensing.

Linbo Luo received the B.S. degree in electronics and information engineering from the China University of Geosciences, Wuhan, China, in 2002, the M.S. degree in engineering of traffic information and control from the Wuhan University of Technology, Wuhan, in 2005, and the Ph.D. degree from the Department of Electronic and Computer Science, Hanyang University, Seoul, South Korea, in 2012.

From 2014 to 2019, he was an Associate Professor with the China University of Geosciences. His research interests include image processing, image warping, and digital image stabilization.

Wenping Gong received the B.S. degree in civil engineering from Tongji University, Shanghai, China, in 2011, and the Ph.D. degree in civil engineering from Clemson University, Clemson, SC, USA, in 2014.

From 2015 to 2017, he was a Research Assistant Professor with the Glenn Department of Civil Engineering, Clemson University. He is currently a Professor with the Faculty of Engineering, China University of Geosciences, Wuhan, China. He has authored or coauthored more than 30 papers in various peer reviewed international journals, including *Engineering Geology*. His research interests include uncertainty, reliability, and risk in geological and geotechnical engineering; slope and landslide analysis and risk assessment; and tunneling and underground construction.

Dr. Gong was the recipient of the Excellent Paper Award from the Journal of GeoEngineering and the Best Paper Award from GeoShanghai 2014 International Conference. He is currently on the Editorial Boards of Several International Journals, in terms of *Engineering Geology*, *Bulletin of Engineering Geology,* and the *Environment, Marine Georesources and Geotechnology*, and the *International Journal of Geotechnical Engineering*. He is also an Assistant Editor of *Engineering Geology*.

Yong Wang received the Ph.D. degree in pattern recognition and intelligent systems from the Huazhong University of Science and Technology, Wuhan, China, in 2009.

He is currently an Associate Professor with the China University of Geosciences, Wuhan, China. His current research interests include wireless sensor networks and image processing.